Astronomy & Astrophysics manuscript no. sstars2021
September 15, 2021

Letter to the Editor

The mass distribution in the Galactic Centre from interferometric astrometry of multiple stellar orbits

GRAVITY Collaboration⋆: R. Abuter[8], A. Amorim[6,14], M. Bauböck[1,17], J.P. Berger[5,8], H. Bonnet[8], G. Bourdarot[5,1], W. Brandner[3], V. Cardoso[14,16], Y. Clénet[2], Y. Dallilar[1], R. Davies[1], P.T. de Zeeuw[12,1], J. Dexter[15], A. Drescher[1], A. Eckart[4,11], F. Eisenhauer[1], N.M. Förster Schreiber[1], P. Garcia[7,14], F. Gao[18,1], E. Gendron[2], R. Genzel[1,13], S. Gillessen[1], M. Habibi[1], X. Haubois[9], G. Heißel[2], T. Henning[3], S. Hippler[3], M. Horrobin[4], L. Jochum[9], L. Jocou[5], A. Kaufer[9], P. Kervella[2], S. Lacour[2], V. Lapeyrère[2], J.-B. Le Bouquin[5], P. Léna[2], D. Lutz[1], T. Ott[1], T. Paumard[2], K. Perraut[5], G. Perrin[2], O. Pfuhl[8,1], S. Rabien[1], G. Rodríguez-Coira[2], J. Shangguan[1], T. Shimizu[1], S. Scheithauer[3], J. Stadler[1], O. Straub[1], C. Straubmeier[4], E. Sturm[1], L.J. Tacconi[1], K.R.W. Tristram[9], F. Vincent[2], S. von Fellenberg[1], F. Widmann[1], E. Wieprecht[1], E. Wiezorrek[1], J. Woillez[8], S. Yazici[1,4], and A. Young[1]

(Affiliations can be found after the references)

Draft version September 15, 2021

ABSTRACT

The stars orbiting the compact radio source Sgr A* in the Galactic Centre are precision probes of the gravitational field around the closest massive black hole (candidate). In addition to adaptive optics assisted astrometry (with NACO@VLT) and spectroscopy (with SINFONI@VLT, NIRC2@Keck and GNIRS@Gemini) over almost three decades, since 2016/2017 we have obtained 50-100 μas astrometry with the four-telescope interferometric beam combiner instrument GRAVITY@VLT. In this paper we combine the astrometry and spectroscopy of four stars currently going through their pericentre passages, for a high precision determination of the gravitational potential around Sgr A*. The data are in excellent agreement with general relativity orbits around a single central point mass, $M_\bullet = 4.30 \times 10^6 M_\odot$ with a precision of about ±0.25%. From posterior fitting and MCMC Bayesian analysis with different weighting schemes and bootstrapping we improve the significance of our detection of the Schwarzschild precession in the S2 orbit to 7σ, $f_{\rm SP} = 1.00 \pm 0.14$. An extended mass inside S2's apocentre ($\approx 0.23''$ or $2.4 \times 10^4 R_{\rm S}$) must be $\lesssim 3000 M_\odot (1\sigma)$, or $< 0.1\%$ of $M_\bullet$. Adding the enclosed mass determinations from 13 stars orbiting Sgr A* at larger radii, the innermost radius at which the enclosed mass tentatively starts to exceed the mass of Sgr A* is at $\approx 2.5'' \geq 10$ times the apocentre of S2. The excess is at a level of 0.3% of $M_\bullet$, or $\approx 10^4 M_\odot$). These limits and detections are in excellent agreement with the stellar mass distribution (including stellar mass black holes) obtained from the spatially resolved stellar luminosity function.

Key words. black hole physics – Galaxy: nucleus – gravitation – relativistic processes

1. Introduction

The GRAVITY instrument on the Very Large Telescope Interferometer has enabled monitoring the positions of stars within 0.1" from Sgr A* at the Galactic Centre (GC) with $\approx 50\mu$as precision (Gravity Collaboration et al. 2017). The GRAVITY data taken in 2017-2019 together with the adaptive optics (AO) and Speckle data sets obtained since 1992 (at ESO telescopes) or 1995 (at the Keck telescopes) have delivered exquisite coverage of the 16-year, highly elliptical orbit of the star S2, which passed pericentre in May 2018. Besides direct determinations of the mass of Sgr A* ($M_\bullet$) and the distance to the GC (R_0), the interferometric data have provided definitive evidence for general relativistic effects caused by the central massive black hole (MBH) on S2, namely the gravitational redshift and the prograde relativistic precession (Gravity Collaboration et al. 2018a, 2019, 2020, 2021; Do et al. 2019).

Due to its short period and relative brightness, S2 is the most prominent star in the GC, but ever higher quality, high-resolution imaging and spectroscopy of the nuclear star cluster over almost three decades have delivered orbit determinations for ≈ 50 stars (Schödel et al. 2002; Ghez et al. 2003, 2008; Eisenhauer et al. 2005; Gillessen et al. 2009; Gillessen et al. 2017; Schödel et al. 2009; Meyer et al. 2012; Boehle et al. 2016). The motions of these stars show that the gravitational potential is dominated by a compact source of $\approx 4.3 \times 10^6 M_\odot$ concentrated within S2's pericentre distance of 14 mas, or 120 AU, and 1400 times the event horizon radius $R_{\rm S}$ of a Schwarzschild (non-rotating) MBH for a distance of 8.28 kpc (Gravity Collaboration et al. 2019, 2021).

S2 passes pericentre at 120 AU ($\approx 1400\, R_{\rm S}$) with a mildly relativistic orbital speed of 7700 km/s ($\beta = v/c = 0.026$). From monitoring the star's radial velocity and motion on the sky from data taken prior to and up to two months after pericentre, Gravity Collaboration et al. (2018a) were able to detect the first post-Newtonian effects of GR, the gravitational redshift, along with the transverse Doppler effect of special relativity. The combined effect for S2 shows up as a 200 km/s residual centred on the pericentre time, relative to the Keplerian orbit with the same parameters. Gravity Collaboration et al. (2019) improved the statistical robustness of the detection of the gravitational redshift to 20σ. Do et al. (2019) confirmed these findings from a second,

⋆ GRAVITY is developed in a collaboration by the Max Planck Institute for extraterrestrial Physics, LESIA of Paris Observatory / CNRS / Sorbonne Université / Univ. Paris Diderot and IPAG of Université Grenoble Alpes / CNRS, the Max Planck Institute for Astronomy, the University of Cologne, the CENTRA - Centro de Astrofisica e Gravitação, and the European Southern Observatory. Corresponding authors:

independent data set mainly from the Keck telescope. While the gravitational redshift occurs solely in wavelength space, the superior astrometry of GRAVITY sets much tighter constraints on the orbital geometry, mass and distance, thus decreasing the uncertainty more than three times relative to data sets constructed from single-telescope, AO imaging and spectroscopy.

The precession induced by the Schwarzschild metric leads to a prograde rotation of the orbital ellipse in its plane of $\Delta\omega = 12.1'$ per revolution for S2, corresponding to a shift in the milliarcsec regime of the orbital trace on sky, and hence the advantage of using interferometry is obvious. Gravity Collaboration et al. (2020) detected the Schwarzschild precession at the 5σ level. The uncertainties on the amount of precession can then be interpreted as limits on how much extended mass (leading to retrograde precession) might be present within the S2 orbit.

Here, we expand our previous analysis by two more years, to 2021.6. Further, we combine in our analysis GRAVITY data from four stars, alongside with the previous AO data. Section 2 presents the new data and section 3 describes our analysis. In Section 4 we show the combined fits, improving the accuracy of the measured post-Newtonian parameters of the central black hole, and the limits on the extended mass (Section 5). In combination with earlier measurements of stars with larger apocentres, we study the mass distribution out to ≈ 3". Section 6 summarizes our conclusions.

2. Observations

The interferometric astrometry with GRAVITY has several distinct advantages over single-telescope, AO imaging (Figure 1).

1. The higher angular resolution yields an order of magnitude better astrometric precision for isolated sources.
2. For crowded environments, such as the central arcsecond that has a surface density > 100 stars per square arcsecond to $K < 17$ (and more for fainter limits, Genzel et al. 2003; Baumgardt et al. 2018; Waisberg et al. 2018), the interferometric data sets are much less affected (by a factor of several hundred) by confusion noise. In the context of the GC cluster imaging this issue has been recognized early and discussed (Ghez et al. 2003, 2008; Gillessen et al. 2017; Do et al. 2019; Gravity Collaboration et al. 2020). For modest duration 'orbit crossings' of individual brighter stars this often means that data over a duration of one or up to several years are affected. The situation is much worse at or near pericentre passage of S2 (2002, 2018), when the star and the variable emission from Sgr A* are in the same diffraction beam of an $8 - 10$ m class telescope (Ghez et al. 2008). For the epoch 2021/2022 it is clear that in addition to Sgr A*, three to four stars are present in the central area, making single-telescope astrometry even more uncertain or unusable.
3. Near pericentre, astrometric measurements with interferometry reduce to fitting the phases and visibilities with a double or multiple point source model in a single pointing of the interferometric fibre, which is straightforward and reliable, once the optical aberrations across the fiber field of view are corrected for (Gravity Collaboration et al. 2020, 2021). At larger separations, double pointings of the fibre are required and astrometry requires using the metrology system (appendix A.1.2). In contrast, AO astrometry relies on establishing a reliable reference frame of neighboring stars from a careful correction of the distortion imaging properties of the system (Plewa et al. 2015; Sakai et al. 2019; Jia et al. 2019), which is challenging over long periods.

In addition to S2 (now moving away from Sgr A* since its 2018.38 pericentre), we use the stars S29 ($K = 17.6$, pericentre 2021.41), S38 ($K = 18.3$, pericentre 2022.70) and S55 ($K = 17.2$, pericentre 2021.7). The latter was labeled S0-102 in Meyer et al. (2012), who determined its orbital period to 12 years.

- For S2 we include 128 NACO astrometric data points, 92 SINFONI, 3 Keck (2000-2002), 2 NACO (2003) and 4 GNIRS@GEMINI spectra, and 82 GRAVITY astrometric measurements. Compared to Gravity Collaboration et al. (2020), we have added the 4 GNIRS spectra, and 17 GRAVITY epochs. These data cover the time span 1992.2-2021.6.
- For S29 we include 94 NACO, 17 SINFONI, 2 GNIRS, and 21 GRAVITY measurements, covering 2002.3-2021.6.
- For S38 we include 110 NACO, 10 SINFONI spectra, and 6 GRAVITY measurements, covering 2004.2-2021.6.
- For S55 we include 42 NACO, 2 SINFONI, and 18 GRAVITY measurements, covering 2004.5-2021.6.
- We also analyzed the NACO and SINFONI 2002-2019 data for another 13 $K \approx 12 - 16$ stars with sufficient data to infer an enclosed mass (and their orbital parameters), with the GC distance fixed to $R_0 = 8279$ pc (i.e. using the best fitting four-star orbit, see Sec. **??**). Following Gravity Collaboration et al. (2020) we established in these cases the reference frame (x_0, y_0, vx_0, vy_0) from 75 NACO measurements of the position of Sgr A*(IR) between 2003 and 2019.7, when the central source was in a bright ('flare') state.

3. Analysis

For a single-star fit, we typically have to fit for 14 parameters: The six parameters describing the initial osculating Kepler orbit $(a, e, i, \omega, \Omega, t_0)$, the distance and central mass, the five coordinates describing the position on the sky and the three-dimensional velocity of the reference (relative to the AO spectroscopic/imaging frame), and a dimensionless parameter encoding the non-Keplerian effect we are testing for. For the gravitational redshift we used $f_{\rm gr}$, which is 0 for Newtonian orbits and 1 for GR-orbits. In Gravity Collaboration et al. (2018a) we found $f_{\rm gr} = 0.90 \pm 0.17$, and in Gravity Collaboration et al. (2019) $f_{\rm gr} = 1.04 \pm 0.05$. Do et al. (2019) reported $f_{\rm gr} = 0.88 \pm 0.17$.

For the Schwarzschild precession we use the post-Newtonian expansion of Will (2008) and add a factor $f_{\rm SP}$ in the equation of motion in front of the Schwarzschild related terms (Gravity Collaboration et al. 2020), where $f_{\rm SP} = 0$ corresponds to Keplerian motion and $f_{\rm SP} = 1$ to GR. In Gravity Collaboration et al. (2020) we found $f_{\rm SP} = 1.10 \pm 0.19$.

Similarly, we parameterize an extended mass distribution by including a parameter $f_{\rm ext}$ in the normalization of the profile. Following Gillessen et al. (2017) and Gravity Collaboration et al. (2020) we assume a Plummer (1911) profile

$$\rho(r) = \frac{3 f_{\rm Pl} M_\bullet}{4\pi\, a_{\rm Pl}^3} \times \left(1 + \left(\frac{R}{a_{\rm Pl}}\right)^2\right)^{-5/2} \quad (1)$$

with scale length $a_{\rm Pl}$ and total mass $f_{\rm Pl} M_\bullet$. We use $a_{\rm Pl} = 1.27 a_{\rm apo}({\rm S2}) = 0.3''$ (Mouawad et al. 2005). The enclosed mass within R is $M(\leq R) = f_{\rm Pl} M_\bullet (1 + R^2/a_{\rm Pl}^2)^{-3/2}$. We fit for the fraction of $M_\bullet$ that is in the extended mass, $f_{\rm Pl}$.

The 14 parameters all have uncertainties and show correlations. In particular, distance and mass are uncertain and correlated. Following Gravity Collaboration et al. (2018a, 2019, 2020) we find the best-fit values (including, for instance $f_{\rm SP}$, or the mass of a second, extended Plummer mass component)

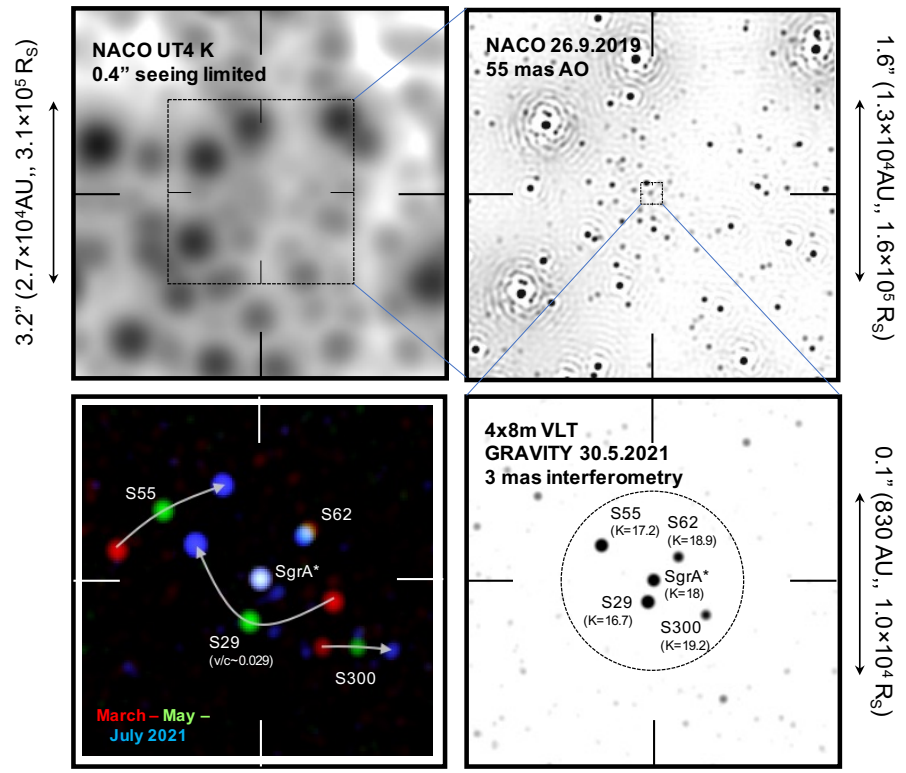

Fig. 1. Progress in stellar astrometric imaging in the GC, from seeing limited observations ($\approx 0.4-0.5''$ FWHM, top left), to AO imaging on 8−10 m class telescopes (50 − 60 mas FWHM, $\approx$ 300 − 500 μas astrometry, top right), to current quality interferometric imagery with GRAVITY@VLTI (bottom panels, 2×4 mas FWHM resolution, 30 − 100 μas astrometry). Bottom right: the central $0.2''$ ($2\times10^4 R_S(4.3\times10^6 M_\odot)$) region centered on Sgr A*(IR) on May 30, 2021 (see Appendix A.2, Gravity Collaboration 2021a). During 2021 the central GRAVITY field of view was dominated by four stars (S29, S55, S62 and S300) with K-band magnitudes between 16.7 and 19.2, in addition to variable emission from Sgr A*(IR) itself. The dashed circle indicates the field-of-view of GRAVITY, defined by the Gaussian acceptance profile of the pick-up fibres in the instrument. Comparing in the bottom left panel three such images taken on March 30 (red), May 30 (green) and July 26 (blue), the orbital motions of all four stars are easily seen, topped by the $\approx$ 8740 km/s velocity of S29 at its pericentre on 2021.41 ($R_{\rm peri} \approx 90$ AU).

a posteriori, fitting for the optimum values of all parameters, including prior constraints. The inferred uncertainties are affected and partially dominated by systematics, especially when combining the evidence from three or more measurement techniques.

Further, we carried out a Markov-Chain Monte Carlo analysis. Using 100 000 realizations we find the distributions and parameter correlations of the respective dimensionless parameter $f_{\rm SP}$ or $f_{\rm Pl}$ with the other parameters and test whether their distribution are well described by Gaussians.

For a more details on our data analysis see Gravity Collaboration et al. (2018a, 2019, 2020, 2021) and Appendix A.

In Gillessen et al. (2009); Gillessen et al. (2017) we consistently found that the basic parameters describing the gravitational potential (central mass $M_\bullet$ and extended mass, for instance $M_{\rm Pl}(< R_{\rm Pl})$ for an assumed Plummer distribution of scale radius $R_{\rm Pl}$), as well as GC distance R_0, are best constrained by the S2 data alone. Including other stars only moderately improved the fitting quality and uncertainties. This is because of the superior number and quality of the S2 data compared to those of the other stars. Since the availability of the superior GRAVITY astrometry S2 completely dominated our knowlegde about the central potential. Another reason is that only for S2 we had data at/near pericentre, which are most sensitive to the mass distribution, as the explicit analysis in (Gillessen et al. 2017) shows.

This situation has changed with the data set here. We now have GRAVITY data of four stars with comparable pericentres at 12 mas (S29) 14 mas (S2), 26 mas (S38) and 29 mas (S55). Naturally one needs to fit for 4 × 6 orbital parameters $(a_i, e_i, i_i, \omega_i, \Omega_i, t_{0,i})$, in addition to the NACO/SINFONI zero points $(x_0, y_0, vx_0, vy_0, vz_0)$, and $M_\bullet$, as well as $f_{\rm SP}$ and/or $M_{\rm ext}(< R_{\rm ext})$. Yet, the inclusion of near-pericentre GRAVITY data of S29, S38 and S55 decreases parameter correlations and uncertainties (Figure 2), also because the orbits are oriented almost perpendicular to each other in at least one of the Euler angles.

In Gravity Collaboration et al. (2020) we combined the zero point priors of Plewa et al. (2015) and the locations/drifts of the flare positions. Here we use in addition the information of a sample of stars with orbits that have a sufficient phase coverage to constrain the zero points. Using 13 stars, we derive $x_0 = (-5.7 \pm 1.5) \times 10^{-4}$ as, $y_0 = (-0.55 \pm 2.5) \times 10^{-4}$ as (both epoch 2010.35), $vx_0 = (6.3 \pm 0.7) \times 10^{-5}$ as/yr, $vy_0 = (3.3 \pm 0.2) \times 10^{-5}$ as/yr, consistent with the earlier estimates, but with smaller uncertainties.

4. Schwarzschild precession for S2

Repeating the analysis of Gravity Collaboration et al. (2020) (S2 alone but with the updated zero points) and solving for the Schwarzschild precession parameter we find $f_{\rm SP} = 0.85 \pm 0.16$ ($\chi^2_r = 1.11$, $\chi^2 = 543$) and $f_{\rm SP} = 1.23 \pm 0.14$ ($\chi^2_r = 1.70$, $\chi^2 = 1076$) if the S2 data plus the flare positions of Sgr A* are considered. This is naturally very similar to the results of Gravity Collaboration et al. (2020), but the new data have decreased the 1σ uncertainty from ±0.19 to ±0.16.

Next we fit with the four star (S2, S29, S38, S55) data, and find $f_{\rm SP} = 0.997 \pm 0.144$, with $\chi^2_r = 2.17$, $\chi^2 = 2344$ (Figure 2).

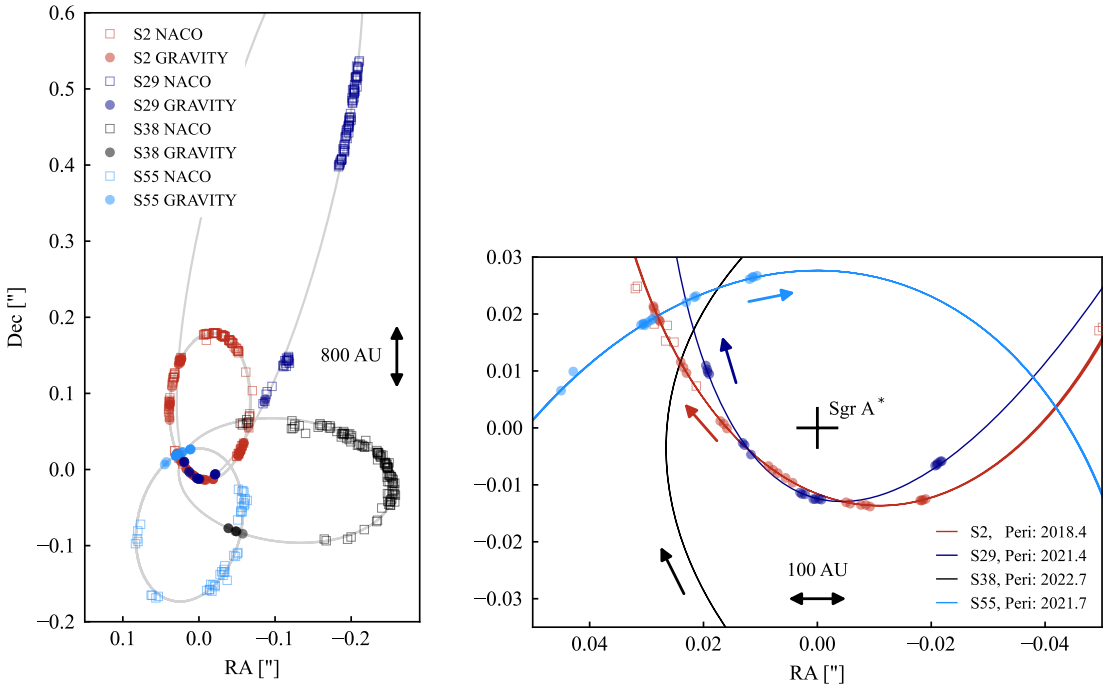

Fig. 2. Summary of the 1992-2021 astrometric data for the stars S2 (blue (NACO) and black (GRAVITY), 2002-2016 best fitting orbit in cyan, 2017-2022 best fitting orbit in dark blue), S29 (open red squares (NACO) and brown filled squares (GRAVITY), with red/orange best fitting orbit), S38 (open green (NACO) and filled green squares (GRAVITY), with green best fitting orbit), and S55 (open magenta triangles (NACO) and filled magenta squares (GRAVITY), with grey best fitting orbit). The black cross marks the position of the compact radio source Sgr A* and mass centre. The directions of projected orbital motions are marked by arrows.

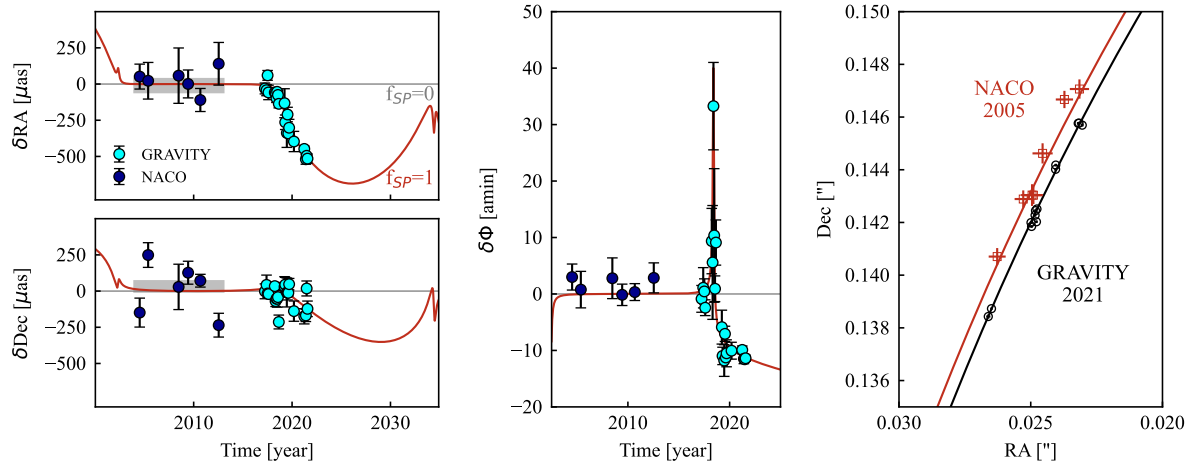

Fig. 3. Posterior analysis of all data by fitting for $f_{\rm SP}$ simultaneously with all other parameters. The two left panels show the residuals in RA (top) and Dec (between) between the GRAVITY (cyan filled black circles, and 1σ uncertainties) and NACO data (black filled circles, and 1σ uncertainties) and the best GR fit (red curve, $f_{\rm SP}$ = 1.00, Rømer effect, plus special relativity, plus gravitational redshift and Schwarzschild precession), relative to the same orbit for $f_{\rm SP}$ = 0 (Kepler/Newton, plus Rømer effect, plus special relativity, plus gravitational redshift). The orbital elements for non-Keplerian orbits (i.e. with $f_{\rm SP} \neq 0$) are interpreted as osculating parameters at around the apocentre time, 2010.35. NACO and GRAVITY data are averages of several epochs. The grey bars denote averages over all NACO data near apocentre (2004-2013). The middle panel shows the same for the residual orbital angle on the sky $\delta\phi = \phi(f_{\rm SP} = 1) - \phi(f_{\rm SP} = 0)$. Right: Zoom into the 2005/2021 part of the S2 orbit, plotted in the mass rest frame. The earlier orbital trace does not coincide with the current one due to the Schwarzschild precession.

Figure 3 shows the residuals of the best fits and the data from the corresponding Newtonian ($f_{\rm SP}$ = 0) orbit. The combination of the near-pericentre GRAVITY data of four stars improves the fitting results of the common parameters. The contributions raising $\chi^2_r > 1$ come from the NACO data of S29, S38 and S55 covering the outer parts of their orbits. These data are more affected by source confusion, and we henceforth used the outlier robust fitting outlined in Gravity Collaboration et al. (2020).

Applying MCMC analysis to the two cases we find the most likely values of $f_{\rm SP} = 0.85 \pm 0.18$ (S2 alone) and $f_{\rm SP} = 0.99 \pm 0.15$ (S2, S29, S38, S55). Figure B.1 shows the large set of parameter correlations, including the well known degeneracy between mass

and distance (Ghez et al. 2008; Boehle et al. 2016; Gillessen et al. 2009; Gillessen et al. 2017). It is worth noting that all of the 32 parameters of the four-star fit are well constrained.

As discussed by Gravity Collaboration et al. (2020) the impact of the high eccentricity of the S2 orbit ($e = 0.88$) is that most of the precession happens in a short time-frame around pericentre. Due to the geometry of the orbit most of the precession shows up in the RA-coordinate, and the change in ω after pericentre appears as a kink in the RA-residuals. The data are obviously in excellent agreement with GR. Compared to Gravity Collaboration et al. (2020) the significance of this agreement has improved from 5 to 7.5 σ, from the combination of adding two more years of GRAVITY data to the S2 data set and the expansion to a four-star fit. Table B.1 gives the best fit orbit parameters, zero points, central mass and GC distance.

As of 2021, S2 is sufficiently far away from pericentre, such that the Schwarzschild precession can now be seen as a ≈ 0.6 mas shift between the data sets in RA (and less so in Dec) between two consecutive passages of the star on the apocentre-side of the orbit. This effect is obvious when comparing the 2021 GRAVITY data to the 2005 NACO data, exactly one period prior (Figure 3 right). This comparison illustrates that the Schwarzschild precession dominates the entire orbit and that there is no detectable retrograde (Newtonian) precession due to an extended mass component (see Heißel et al. 2021).

5. Limits on extended mass

In the following we fix $f_{\rm SP} = 1$ at its GR value and allow instead for an extended mass component parameterized by $f_{\rm Pl}$. We find $f_{\rm Pl} = (2.7 \pm 3.5) \times 10^{-3}$ from a single S2 fit, and $f_{\rm Pl} = (-3.8 \pm 2.4) \times 10^{-3}$ for the four-star fit. The latter 1σ error is consistent with but 3-4 times smaller than that of Gillessen et al. (2017) and 1.7 times smaller than that of Gravity Collaboration et al. (2020). In Figure 4 we included the 3σ uncertainty as a conservative upper limit, indicating that the extended mass cannot exceed $7500 M_\odot$ within the apocentre of S2. As in Gillessen et al. (2017) and Gravity Collaboration et al. (2020) we find again that varying $a_{\rm Pl}$ or replacing the Plummer distribution by a suitable power law changes this result by only small amounts. Further, we get a weaker limit by a factor of ≈ 2 when omitting the NACO astrometry, using thus only GRAVITY & SINFONI data.

(Heißel et al. 2021) have pointed out that the impact of an extended mass is naturally largest near apocentre of the orbit. Figure C.2 shows the impact of adding various amounts of extended mass on top of the best-fit residuals with a point mass only. Our data are just commensurate with an additional $f_{\rm Pl} = 0.25\%$ of $M_\bullet$, but a larger mass is excluded by both the near-peri- and near-apocentre data. The apparent sensitivity of the near-pericentre data in Figure C.2 is the result of referring the residuals to the osculating Keplerian orbit at apocentre in 2010.35, such that the accumulating retrograde precession enters the near-pericentre data.

A second, independent measure of the dynamically inferred mass distribution comes from fitting for the central mass using 13 individual stellar orbits with $a = 0.1''$ to $3.8''$ (Gillessen et al. 2017), with the distance and zero-points fixed to the best fitting values of the four-star fit (Figure C.1). We then averaged the results in three groups of four stars with $0.11'' < a < 0.22''$, five stars with $0.27'' < a < 0.4''$, three stars between $0.55''$ and $1.6''$, and two stars between $1.6''$ and $3.8''$. Most of the stars in the first two groups are classical 'S-stars' (most are early type B stars) with typically large eccentricities (e.g. Ghez et al. 2008; Gillessen et al. 2017), while most of the stars in the third group are O and B stars in the clock-wise disk (Paumard et al. 2006; Bartko et al. 2009; Lu et al. 2009), which have modest or small eccentricities. The stars in the first two groups indicate that the mass is consistent with $M_\bullet$, to within 0.3-0.6%. There is no indication for an extended mass larger than $\approx 25,000 M_\odot$ within $2a_{\rm apo}(\rm S2) \approx 0.5''$. The outermost group of stars suggests an extended mass of $15,000 M_\odot$ (and conservatively a 3σ limit of $50,000 M_\odot$ within $5 - 10\, a_{\rm apo}(\rm S2)$.

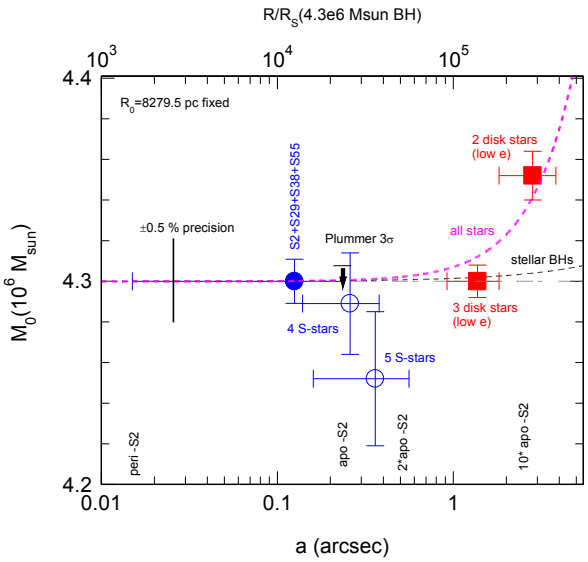

Fig. 4. Summary of the central mass distribution in the GC, within about ten times the apocentre radius of the S2 orbit, $\approx 2.5''$. The innermost filled blue circle is the central mass of $4.30 \times 10^6 M_\odot$ (for $R_0 = 8279$ pc, and its 1σ uncertainty of $12,000 M_\odot$), which the four-star fitting here has established to lie within the $1200 R_{\rm S}$ pericentre of S29. The second filled blue circle denotes the 3σ upper limit of $M_{\rm ext}(\leq 0.3'')$ of the sum of $M_\bullet$ and any extended Plummer mass of assumed scale radius 0.3". The two open blue circles and two red filled squares show averages of enclosed masses within the semi-major axes of other S-stars and clock-wise disk stars. The (expected) contribution of stellar mass black holes at $\approx 1''$ is denoted by a black arrow (Baumgardt et al. 2018). The blue, dashed line is the sum of $M_\bullet$ and the extended stellar mass distribution from the literature (e.g. Genzel et al. 2010; Alexander 2017; Schödel et al. 2018; Baumgardt et al. 2018. All data are in excellent agreement with a point mass (the MBH Sgr A*) and a dense star cluster with a power law density slope $\gamma \approx 1.6$, consisting of main-sequence stars and giants, with a small contribution of giants. No extra component from dark matter or an intermediate mass black hole $> 10^3 M_\odot$ (Gravity Collaboration 2021b) is required or compatible with the data.

Figure 4 summarizes the mass distribution within $5''$ ($\approx 20\times$ the apocentre of S2). These estimates and limits are in excellent agreement with the distribution of stars (and stellar mass black holes and neutron stars) contained in this inner region around Sgr A*, as estimated from models and simulations (Alexander 2017; Baumgardt et al. 2018), or from observations of faint stars and diffuse stellar light (Figure 4, Genzel et al. 2010; Gallego-Cano et al. 2018; Schödel et al. 2018; Habibi et al. 2019.

In summary, several precise (O(0.1-0.3%), 1σ) determinations show that the mass distribution in the GC within 5" $\approx 5 \times 10^5 R_{\rm S}$ of Sgr A* is dominated by a central mass. This mass is definitely enclosed within the pericentre of S29 (12 mas, $\approx 1200 R_{\rm S}$). Taking the gas motions at $\approx 3 - 5\, R_{\rm S}$ (Gravity Collaboration et al. 2018b) and the mm-size of Sgr A* (Doeleman et al. 2008; Johnson et al. 2017; Issaoun et al. 2019) into account, the data are in excellent agreement with the MBH paradigm.

6. Conclusions

We have presented GRAVITY astrometry obtained at the VLTI in 2021 for stars orbiting very close to the supermassive black hole Sgr A* at the GC, including S2, S29, S38, S55. New radial velocities were obtained with GNIRS at Gemini North. The analysis of these data leads to the following conclusions.

The star S2 has now returned to the part of its 16-year orbit for which good NACO AO-assisted positions were obtained during its previous passage. A direct comparison of the positions confirms that the orientation of the orbital ellipse has indeed shifted in its plane by the 12.1' expected from the prograde Schwarzschild precession induced by the gravitational field of the MBH, as reported in Gravity Collaboration et al. (2020).

At $K = 14.1$, S2 is comparably bright. With its increased distance in 2021 from Sgr A* we were now able to map the immediate vicinity of the central black hole to significantly fainter objects. This provided accurate positions for S29, S38, S55. These stars have previously measured NACO positions when they were further away from Sgr A*. Combination with the GRAVITY positions improves the orbital parameters of these three stars substantially. S29 is on a deeply plunging ($e = 0.97$) orbit with a period of ≈ 90 years, and pericentre passage on 2021.41, with a space velocity of ≈ 8740 km/s at only 90 AU from Sgr A*.

S2, S29, S38 and S55 orbit in the same gravitational potential, and combining their astrometry and radial velocity data improves the accuracy of the determination of the properties of the central MBH, as characterised by the canonical PPN parameters. This leads to a 14% measurement precision of the Schwarzschild precession, in full agreement with the prediction of GR. The best fit further yields $R_0 = (8277 \pm 9)$ pc and $M_\bullet = (4.297 \pm 0.012) \times 10^6 M_\odot$ (statistical errors, see Gravity Collaboration et al. 2021 for a discussion of the systematics).

Any smooth extended mass distribution would lead to a retrograde precession of the S2 orbit relative to the relativistically precessing one, and we can thus place a limit on a hypothetical mass distribution. The measurement errors leave room for at most $\lesssim 3000\, M_\odot$ in extended mass out to 230 mas. We included a further 13 stars with earlier measurements in an attempt to trace this effect as a function of radius. The data are fully consistent with a single point mass, and only at $r \gtrsim 2.5''$ the enclosed mass tentatively exceeds the mass of Srg A*. This is consistent with the theoretically expected stellar mass distribution.

Our multi-epoch GRAVITY data also confirms that at any time there are likely a few stars sufficiently close to Sgr A* on the sky to systematically influence its position derived with AO-assisted imaging on single telescopes. Also in 2022, two stars will pass the pericenters of their orbits at less than 100 mas distance (S38 and S42). The upgrade of GRAVITY to GRAVITY+ will push the sensitivity limit to $K > 20$, which may reveal further stars with even smaller orbits. The 39 m ELT equipped with MICADO might be the prime choice for obtaining radial velocities of such stars. Yet, GRAVITY+ will beat its angular resolution by a factor three, allowing continued $< 50\,\mu$as astrometry and going even deeper than what we have demonstrated so far (Gravity Collaboration 2021a).

Acknowledgements. We are very grateful to our funding agencies (MPG, ERC, CNRS [PNCG, PNGRAM], DFG, BMBF, Paris Observatory [CS, PhyFOG], Observatoire des Sciences de l'Univers de Grenoble, and the Fundação para a Ciência e Tecnologia), to ESO and the Paranal staff, and to the many scientific and technical staff members in our institutions, who helped to make NACO, SINFONI, and GRAVITY a reality. S.G. acknowledges the support from ERC starting grant No. 306311. F.E. and O.P. acknowledge the support from ERC synergy grant No. 610058. The GNIRS spectra were obtained at the international Gemini Observatory, a program of NSF's NOIRLab, managed by the Association of Universities for Research in Astronomy (AURA) under a cooperative agreement with the National Science Foundation (NSF) on behalf of the Gemini Observatory partnership: the National Science Foundation (United States), National Research Council (Canada), Agencia Nacional de Investigación y Desarrollo (Chile), Ministerio de Ciencia, Tecnología e Innovación (Argentina), Ministério da Ciência, Tecnologia, Inovações e Comunicações (Brazil), and Korea Astronomy and Space Science Institute (Republic of Korea). This work was enabled by observations made from the Gemini North telescope, located within the Maunakea Science Reserve and adjacent to the summit of Maunakea. We are grateful for the privilege of observing the Universe from a place that is unique in both its astronomical quality and its cultural significance.

References

Alexander, T. 2017, ARA&A, 55, 17
Arras, P., Bester, H. L., Perley, R. A., et al. 2020, arXiv e-prints, arXiv:2008.11435
Baron, F., Monnier, J. D., & Kloppenborg, B. 2010, in Society of Photo-Optical Instrumentation Engineers (SPIE) Conference Series, Vol. 7734, Optical and Infrared Interferometry II, ed. W. C. Danchi, F. Delplancke, & J. K. Rajagopal, 77342I
Bartko, H., Martins, F., Fritz, T. K., et al. 2009, ApJ, 697, 1741
Baumgardt, H., Amaro-Seoane, P., & Schödel, R. 2018, A&A, 609, A28
Boehle, A., Ghez, A. M., Schödel, R., et al. 2016, ApJ, 830, 17
Do, T., Hees, A., Ghez, A., et al. 2019, Science, 365, 664
Doeleman, S. S., Weintroub, J., Rogers, A. E. E., et al. 2008, Nature, 455, 78
Eisenhauer, F., Genzel, R., Alexander, T., et al. 2005, ApJ, 628, 246
Enßlin, T. A. 2019, Annalen der Physik, 531, 1800127
Gallego-Cano, E., Schödel, R., Dong, H., et al. 2018, A&A, 609, A26
Genzel, R., Eisenhauer, F., & Gillessen, S. 2010, Rev. Mod. Phys., 82, 3121
Genzel, R., Schödel, R., Ott, T., et al. 2003, ApJ, 594, 812
Ghez, A., Duchêne, G., Matthews, K., et al. 2003, ApJ Letters, 586, 127
Ghez, A., Salim, S., Weinberg, N. N., et al. 2008, ApJ, 689, 1044
Gillessen, S., Eisenhauer, F., Trippe, S., et al. 2009, ApJ, 692, 1075
Gillessen, S., Plewa, P. M., Eisenhauer, F., et al. 2017, ApJ, 837, 30
Gravity Collaboration. 2021a, "A&A in prep."
Gravity Collaboration. 2021b, "A&A in prep."
Gravity Collaboration, Abuter, R., Accardo, M., et al. 2017, A&A, 602, A94
Gravity Collaboration, Abuter, R., Amorim, A., et al. 2018a, A&A, 615, L15
Gravity Collaboration, Abuter, R., Amorim, A., et al. 2019, A&A, 625, L10
Gravity Collaboration, Abuter, R., Amorim, A., et al. 2020, A&A, 636, L5
Gravity Collaboration, Abuter, R., Amorim, A., et al. 2018b, A&A, 618, L10
Gravity Collaboration, Abuter, R., Amorim, A., et al. 2021, A&A, 647, A59
Habibi, M., Gillessen, S., Pfuhl, O., et al. 2019, ApJ, 872, L15
Heißel, G., Paumard, T., Perrin, G., & Vincent, F. 2021, "A&A submitted"
Issaoun, S., Johnson, M. D., Blackburn, L., et al. 2019, ApJ, 871, 30
Jia, S., Lu, J. R., Sakai, S., et al. 2019, ApJ, 873, 9
Johnson, M. D., Bouman, K. L., Blackburn, L., et al. 2017, ApJ, 850, 172
Knollmüller, J. & Enßlin, T. A. 2019, arXiv e-prints, arXiv:1901.11033
Lu, J. R., Ghez, A. M., Hornstein, S. D., et al. 2009, ApJ, 690, 1463
Meyer, L., Ghez, A., Schödel, R., et al. 2012, Science, 338, 84
Mouawad, N., Eckart, A., Pfalzner, S., et al. 2005, Astronomische Nachrichten, 326, 83
Paumard, T., Genzel, R., Martins, F., et al. 2006, ApJ, 643, 1011
Plewa, P. M., Gillessen, S., Eisenhauer, F., et al. 2015, MNRAS, 453, 3234
Plummer, H. C. 1911, MNRAS, 71, 460
Sakai, S., Lu, J. R., Ghez, A., et al. 2019, ApJ, 873, 65
Schödel, R., Gallego-Cano, E., Dong, H., et al. 2018, A&A, 609, A27
Schödel, R., Merritt, D., & Eckart, A. 2009, A&A, 502, 91
Schödel, R., Ott, T., Genzel, R., et al. 2002, Nature, 419, 694
Thiébaut, E. 2008, in Society of Photo-Optical Instrumentation Engineers (SPIE) Conference Series, Vol. 7013, Optical and Infrared Interferometry, ed. M. Schöller, W. C. Danchi, & F. Delplancke, 70131I
Waisberg, I., Dexter, J., Gillessen, S., et al. 2018, MNRAS, 476, 3600
Will, C. M. 2008, ApJ, 674, L25

[1] Max Planck Institute for extraterrestrial Physics, Giessenbachstraße 1, 85748 Garching, Germany
[2] LESIA, Observatoire de Paris, Université PSL, CNRS, Sorbonne Université, Université de Paris, 5 place Jules Janssen, 92195 Meudon, France
[3] Max Planck Institute for Astronomy, Königstuhl 17, 69117 Heidelberg, Germany
[4] 1st Institute of Physics, University of Cologne, Zülpicher Straße 77, 50937 Cologne, Germany
[5] Univ. Grenoble Alpes, CNRS, IPAG, 38000 Grenoble, France
[6] Universidade de Lisboa - Faculdade de Ciências, Campo Grande, 1749-016 Lisboa, Portugal
[7] Faculdade de Engenharia, Universidade do Porto, rua Dr. Roberto Frias, 4200-465 Porto, Portugal
[8] European Southern Observatory, Karl-Schwarzschild-Straße 2, 85748 Garching, Germany
[9] European Southern Observatory, Casilla 19001, Santiago 19, Chile
[10] Observatoire de Genève, Université de Genève, 51 Ch. des Maillettes, 1290 Versoix, Switzerland
[11] Max Planck Institute for Radio Astronomy, Auf dem Hügel 69, 53121 Bonn, Germany
[12] Sterrewacht Leiden, Leiden University, Postbus 9513, 2300 RA Leiden, The Netherlands
[13] Departments of Physics and Astronomy, Le Conte Hall, University of California, Berkeley, CA 94720, USA
[14] CENTRA - Centro de Astrofísica e Gravitação, IST, Universidade de Lisboa, 1049-001 Lisboa, Portugal
[15] Department of Astrophysical & Planetary Sciences, JILA, Duane Physics Bldg., 2000 Colorado Ave, University of Colorado, Boulder, CO 80309, USA
[16] CERN, 1 Esplanade des Particules, Genève 23, CH-1211, Switzerland
[17] Department of Physics, University of Illinois, 1110 West Green Street, Urbana, IL 61801, USA
[18] Hamburger Sternwarte, Universität Hamburg, Gojenbergsweg 112, 21029 Hamburg, Germany

Appendix A: Experimental Techniques

Appendix A.1: GRAVITY: Determining astrometric separations

The full width half maximum (FWHM) of the interferometric field of view (IFOV) of GRAVITY is 70 mas. In consequence, not all stars discussed in this paper are observable simultaneously. The star S2 has moved too far away from Sgr A* compared to 2018 to be observable simultaneously with Sgr A*, while the stars S55, S29 (and others, see Gravity Collaboration 2021a) are always observed alongside Sgr A*. Depending on the separation, there are two methods to determine the positions of the stars relative to Sgr A*: single-beam and dual-beam astrometry. Single-beam positions are extracted from pointings, in which more than one source is present in the IFOV. The distances between the stars are extracted by fitting a multi-source model to the visibility amplitude and closure phase, each of which are measured at $\approx$ 10 spectral channels for 6 baselines. This yields relative positions of the sources with respect to each other. Since Sgr A* is visible in all our central frames, for those pointings the relative positions also are the absolute ones, i.e. with respect to the mass centre. If the stars are not observable in a single IFOV we need to observe them separately, and apply the dual-beam technique. For the case of two isolated stars, one interferometrically calibrates the first source with the second. The first source serves as a phase reference relative to which offsets of the second source can be measured.

Appendix A.1.1: Single-beam astrometry

If a star is in the same interferometric field of view as Sgr A* (of interest here in 2021 are S29 and S55), we determine the relative separation between the star and Sgr A* by interferometric model fitting to the visibility amplitude and closure phases in the Sgr A* pointing. This methodology is unchanged to the way a separation is determined in (Gravity Collaboration et al. 2021). We thus take into account the effect of phase aberrations as well as bandwidth smearing (Gravity Collaboration et al. 2020).

Appendix A.1.2: Dual-beam astrometry

If the stars are separated by more than the interferometric field of view of GRAVITY, we measure the separation between the two sources by using one of them as the phase reference for the other target. We use S2 as the phase reference, after having checked that its interferometric observables are consistent with having a single point source in the S2 field of view. The separation between any star and S2 is determined by two vectors:

- the vector by which the field of view was moved between S2 and the star. This vector is measured by the metrology system of GRAVITY monitoring the internal optical path differences
- the phase center offset in the S2-calibrated star observation. It is determined by fitting the visibility phase.

The visibility phase is affected by inaccuracies and systematic uncertainties of the metrology. Such telescope-based errors are inherent to the dual-beam part of the measurement.

Typically, we find more stars than just one in the interferometric field of view. We thus need to take into account the visibility phase signatures induced by the additional stars in the dual-beam measurement. This occurs for example for the Sgr A* pointings (where S29, S55, S62 and S300 are present), but also for S38 pointing (which S60 and S63 being present in the field of view). We thus fit the interstellar separations and the phase center offset simultaneously in order to take into account their degeneracies. Yet the separation vectors are mostly sensitive to the visibility amplitude and the closure phase information from the visibility phase, while the phase center offsets mostly acts as an additional term in the visibility phase.

In this way we can relate all positions to our calibrator source, S2. Hence, we can relate the positions also to Sgr A* by subtracting the star-to-S2 and S2-to-Sgr A* separations.

Telescope-based errors cancel out in the closure phase, and therefore the relative positions of the sources are not affected by phase errors. We find that by fitting the closure phases and the visibility phases with equal weights, we minimize the effect of the telescope-based errors, while still being sensitive to the phase information. In order to average out the phase errors, we calibrate all N frames of a given pointing with all M available S2 frames individually. For each of the $N \times M$ resulting data sets, we determine the phase center position and average the resulting phase center locations. This calibration uncertainty adds a systematic uncertainty of 60 μas, divided by the square root of the number available calibrations.

We further improve the accuracy of our phase center measurement by determining the best fit fringe-tracker and science target separation by fitting the S2 observations with a drifting point source model. This takes into account our imperfect knowledge of the separation prior to the observation. Here we follow the concepts first presented in (Gravity Collaboration et al. 2020). Also for the dual-beam analysis, we account for the effect of phase aberrations and bandwidth smearing when calculating the model visibility phase.

Appendix A.2: GRAVITY: Deep Imaging

To obtain deep, high-resolution images of the GC, we have developed a new imaging code 'GRAVITY-RESOLVE' or G$^{\mathrm{R}}$ (Gravity Collaboration 2021a) which draws from RESOLVE (Arras et al. 2020), a Bayesian imaging algorithm formulated in framework of Information Field Theory (Enßlin 2019), but is custom-tailored to GRAVITY observations of the GC. With the Bayesian forward modeling approach, we are able to address data sparsity and to account for various instrumental effects that render the relation between image and measurement more complicated than the simple Fourier transform of the van-Cittert Zernike theorem. To this end, the algorithm formulates a prior model which permits to draw random samples, processes them with the instrumental response function and evaluates the likelihood to compare the predicted visibilities with the actual measurement. This approach can handle the non-invertible measurement equation and enables to work with non-linear quantities such as closure phases. The exploration of the posterior distribution is done with Metric Gaussian Variational Inference (Knollmüller & Enßlin 2019), and infers the the most likely image jointly with an uncertainty estimate. There already exist some imaging tools for optical/near-IR interferometry which implement such a forward modeling approach such as MIRA (Thiébaut 2008) or SQUEEZE (Baron et al. 2010). Our code differs from them in the details of the measurement equation, the prior model and how the maximization and exploration of the posterior is performed.

In the measurement equation, we implemented all instrumental effects relevant for GRAVITY which are coupling efficiency, aberration corrections (Gravity Collaboration et al. 2021), averaging over finite sized wavelength channels also known as bandwidth smearing, and the practice in optical/near-

IR interferometry to construct the complex visibility as the coherent flux over a baseline divided by the total flux of each of the two telescopes. The latter signifies that the visibility amplitude can be unity at most, but coherence loss can degrade the observed visibility from the theory expectation. This we account for by a self-calibration approach where we infer a time- and baseline-dependent calibration factor jointly with the image.

An appropriate prior model is essential to redress the data sparsity inherent to optical/near-IR interferometry, and we specifically tailor it to GC observations. There, we see Sgr A* as a point source in addition to some relatively bright stars whose approximate positions are known from orbit predictions. For those objects, we directly infer the position and brightness using a Gaussian and a log-normal prior respectively. The variability and polarization of Sgr A* is accounted for by allowing for an independent flux value in each frame and polarization state observed. In the actual image itself, we expect to see few faint, yet unknown, point sources and thus impose the individual pixels to be independent with their brightness following an Inverse Gamma distribution. Note that all sources other than Sgr A*, that is all non-variable sources, could in principle also be attributed to the image. However, modeling them as additional point sources improves convergence and mitigates pixelization errors.

Appendix A.3: GNIRS: Determining radial velocities

In 2021 we had four successful observations with GNIRS at the Gemini observatory. We used the long slit in the K-Band with the 10.44 l/mm grating. The slit was positioned so that we observed S2 and S29 simultaneously. To calibrate the data we used the daytime calibration from the day after the observation, which contains a set of dark frames to determine a bad pixel mask, flat frames, and a wavelength calibration. Additionally, a telluric star was observed right after the observation. To determine the velocity of the stars we used template fitting with a high SNR S2 spectrum, in the same way as we extracted the SINFONI velocities (see Gravity Collaboration et al. 2018a). We were able to detect a velocity for S2 in all four observing nights. As S29 is significantly fainter than S2 we needed excellent conditions to get a detection, which was only possible in two of the four nights.

Appendix B: Fit details

In table B.1 we give the best-fit parameters of the four-star fit, comparing also with similar fits from the literature.

Figure B.1 gives the full posterior of the four-star fit in the form of a corner plot.

Appendix C: Additional figures

In Figure C.1 we show the orbital data of additional S-stars that were auxiliary in this work. Figure C.2 illustrates that our S2 data are compatible at most with an extended mass component of around 0.1% enclosed within the S2-orbit.

Table B.1. Best fit orbit parameters. The line '$M_\bullet\,[10^6 M_\odot]_{8277\,\mathrm{pc}}$' gives the masses rescaled to a common distance of $R_0 = 8277\,\mathrm{pc}$, using $M \propto R_0^2$ (Gillessen et al. 2017).

	this paper		**Grav. Coll 2020**		**Gillessen+ 2017**		**Do+ 2019**	
$M_\bullet\,[10^6 M_\odot]$	4.297	0.012	4.261	0.012	4.280	0.100	3.975	0.058
R_0 [pc]	8277	9	8247	9	8320	70	7959	59
$M_\bullet\,[10^6 M_\odot]_{8277\,\mathrm{pc}}$	4.297	0.012	4.292	0.012	4.236	0.100	4.299	0.063
x_0 [mas]	-0.69	0.10	-0.90	0.14	-0.08	0.37	1.22	0.32
y_0 [mas]	0.18	0.10	0.07	0.12	-0.89	0.31	-0.88	0.34
vx_0 [mas/yr]	0.066	0.006	0.080	0.010	0.039	0.041	-0.077	0.018
vy_0 [mas/yr]	0.009	0.009	0.034	0.010	0.058	0.037	0.226	0.019
vz_0]km/s]	-1.8	1.3	-1.6	1.4	14.2	3.6	-6.2	3.7

	S2		**S38**	
a [as]	0.12495	0.00004	0.14254	0.00004
e	0.88441	0.00006	0.8145	0.0002
i [°]	134.70	0.03	166.65	0.40
Ω [°]	228.19	0.03	109.45	1.00
ω [°]	66.25	0.03	27.17	1.02
t_{peri} [yr]	2018.3789	0.0001	2022.7044	0.0080
	S29		**S55**	
a [as]	0.3975	0.0016	0.10440	0.00005
e	0.9693	0.0001	0.7267	0.0002
i [°]	144.37	0.07	158.52	0.22
Ω [°]	7.00	0.33	314.94	1.14
ω [°]	205.79	0.33	322.78	1.13
t_{peri} [yr]	2021.4104	0.0002	2021.6940	0.0083

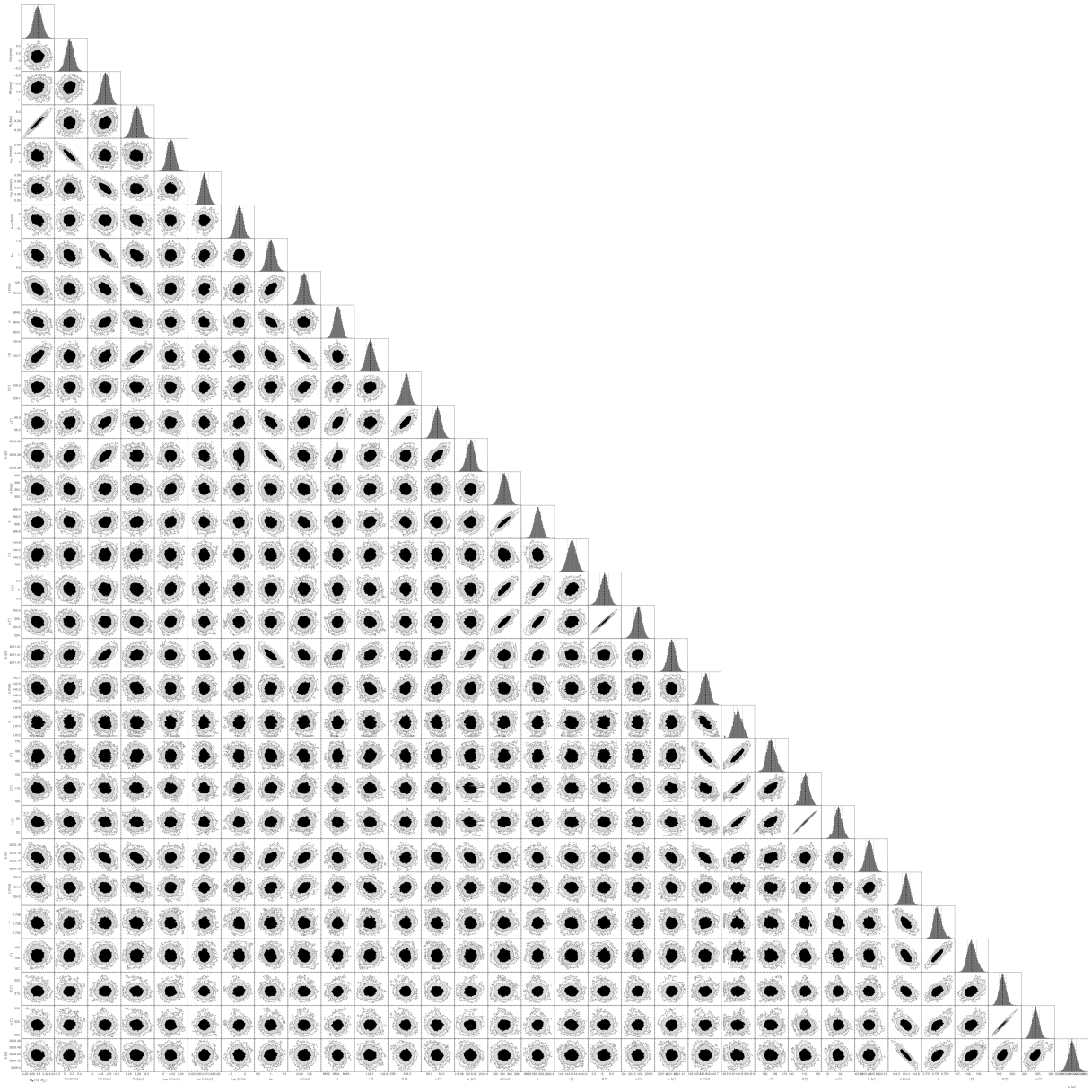

Fig. B.1. Corner plot of the full 32-dimensional parameter space of the four-star fit, consisting of the central mass $M_\bullet$, the distance R_0, the precession parameter $f_{\rm SP}$, the five coordinate system parameters and six orbital elements for each of the four stars used.

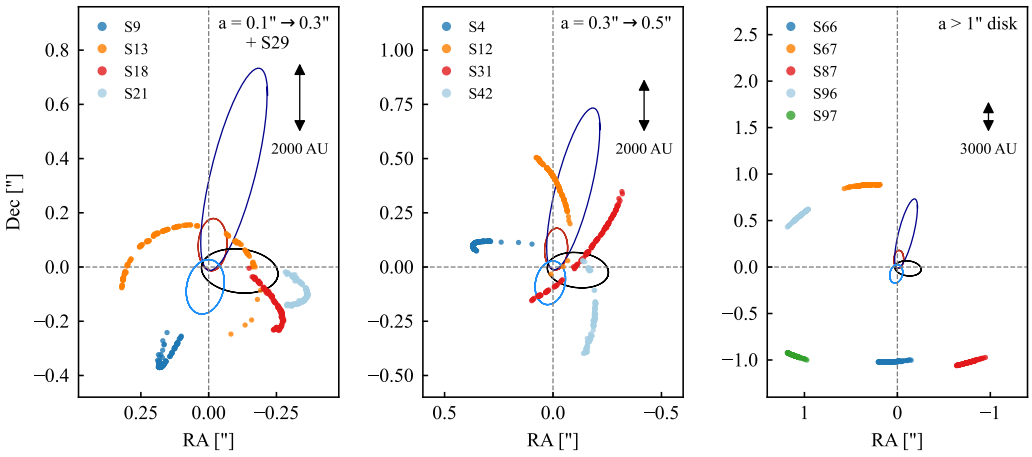

Fig. C.1. Visualization of the orbital (astrometric) data used in determining the mass distribution in the GC. The panels group the stars according to the semi-major axes of their orbits, as indicated in the top left in each panel. For reference, we show in each panel the orbits from the four-star fit. Left: Orbital data for S9, S13, S18 and S21. Middle: S4, S12, S31 and S42. Right: S66, S67, S87, S96 and S97. These data are complemented by multi-epoch spectroscopy for the orbital fitting.

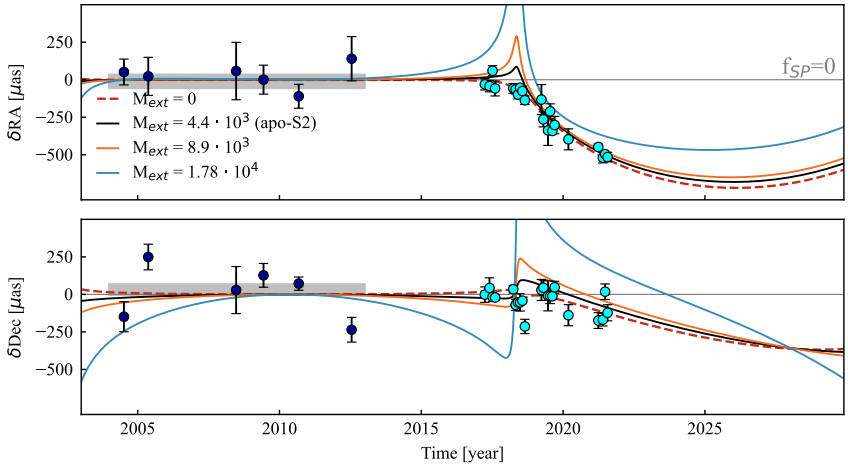

Fig. C.2. Same data and RA-/Dec-residual plots as the left panels in Figure 3, with the dashed red curve denoting the $f_{\rm SP} = 1$ GR curve for the best fitting orbit and mass. In addition, we show orbital models with the same central mass, distance and orbital parameters but now adding an extended mass component assumed to have a Plummer shape (Gillessen et al. 2017) showing the impact of adding a Plummer mass of $M_{\rm ext}$ within the 0.25″ apocentre radius of S2. Black, blue and green curves show the changes expected if this extended Plummer mass is 0.1, 0.3 and 0.6% of $M_\bullet$ (4.4×10^3, 8.9×10^3 and $1.78 \times 10^4 M_\odot$ within the apocentre of S2, $R_{\rm apo} = 0.24''$). Formal fitting shows that no extended mass greater than about $\approx 0.1\%$ of $M_\bullet$ is compatible with the data.